Isoscalar dipole excitations in ^{1}O

AUTHOR(S):

Kanada-En'Yo, Yoshiko; Shikata, Yuki

CITATION:

Kanada-En'Yo, Yoshiko ...[et al]. Isoscalar dipole excitations in ^{1}O. Physical Review C 2019, 100(1): 014301.

ISSUE DATE:

2019-07-01

URL:

http://hdl.handle.net/2433/243335

Isoscalar dipole excitations in ^{16}O

Yoshiko Kanada-En'yo and Yuki Shikata
Department of Physics, Kyoto University, Kyoto 606-8502, Japan

(Received 9 March 2019; published 1 July 2019)

Isoscalar (IS) monopole and dipole excitations in ^{16}O were investigated by the method of shifted basis antisymmetrized molecular dynamics combined with the generator coordinate method. Significant strengths of the IS monopole and dipole transitions were obtained in the low-energy region below the giant resonances. In addition to the compressive mode, which mainly contributes to the high-energy strengths for the IS dipole giant resonance, we obtained a variety of low-energy dipole modes such as the vortical dipole mode in the 1^-_1 state of the vibrating tetrahedral 4α and the $^{12}\mathrm{C}+\alpha$ cluster structure in the 1^-_2 state. The 1^-_1 state contributes to the significant low-energy strength of the IS dipole transition as 5% of the energy-weighted sum rule, which describes well the experimental data observed by the α inelastic scattering.

DOI: 10.1103/PhysRevC.100.014301

I. INTRODUCTION

In the past decades, low-energy monopole and dipole excitations have been attracting great interests (see, for example, reviews in Refs. [1–5] and references therein). A central issue is possible appearance of new excitation modes decoupled from collective vibration modes corresponding the giant resonances (GRs). In experiments with α inelastic scattering extensively performed for study of isoscalar (IS) monopole and dipole excitations, significant low-energy strengths with the fraction of several percentages of the energy-weighted sum rule have been observed in various stable nuclei such as ^{16}O, ^{40}Ca, and ^{208}Pb [6–8]. The questions to be answered are what is the origin of these IS low-energy dipole (LED) strengths and how the dipole modes come down to the energy much lower than the IS giant dipole resonances (GDRs).

In order to understand the IS LED strengths, the vortical dipole (VD) mode (called also the torus or toroidal mode) has been studied first with hydrodynamical models [9,10], and later with microscopic approaches [2,11–18]. The VD mode is characterized by the nuclear vorticity and has a unique feature different from the standard IS dipole mode so-called compressive dipole (CD) in the IS GDR. Since the nuclear density is conserved in the VD mode, its energy can be lower than the IS GDR involving compression of nuclear density. As a measure of the nuclear vorticity in the dipole excitations, the toroidal dipole (TD) operator has been introduced [9,19]. The TD operator is given by the rotational component (a curl term) of the transition current density and the counterpart of the compressive dipole (CD) operator with the irrotational component (a divergence term) of the transition current density, and has been proved to be a good probe for the low-energy VD mode [14].

In light nuclei, also cluster states may contribute to the low-energy IS monopole (IS0) and dipole (IS1) transition strengths because the IS0 and IS1 operators contain higher-order $r^{\lambda+2}$ terms and can excite not only the compressive vibration modes but also the intercluster motion in the cluster states as pointed out by Yamada *et al.* [20] and Chiba *et al.* [21]. Indeed, the low-energy IS monopole strengths in ^{16}O have been described well by cluster states with a semimicroscopic 4α-cluster model [20]. It is an important issue to clarify the IS dipole excitations in ^{16}O, in particular, the cluster and vortical aspects of the low-energy modes.

Theoretical calculations with cluster models have been performed for ^{16}O and suggested a variety of cluster structures such as the tetrahedral 4α and $^{12}\mathrm{C}+\alpha$ structures [20,22–37]. However, there have been no microscopic calculation that successfully describes the energy spectra of ^{16}O. Recently, we applied a microscopic model of the antisymmetrized molecular dynamics (AMD) [38–41] to ^{16}O, and obtained reasonable reproduction of the energy spectra of ^{16}O such as 0^+_2, 2^+_1, 4^+_1, 1^-_2, and 3^-_2 states in the positive- and negative-parity bands with the $^{12}\mathrm{C}+\alpha$ structure and 3^-_1 and 4^+_2 states in the ground band with the tetrahedral 4α structure [36,42].

Our aim is to investigate the IS dipole excitations in ^{16}O. Main interest are properties of the IS LED modes such as the cluster and vortical aspects. For this aim, we apply the method of the shifted basis AMD (sAMD) [43–45] combined with the cluster generator coordinate method (GCM). The sAMD+GCM has been recently constructed to describe both the single-particle excitation and large amplitude cluster mode. This method has been applied to ^{12}C to discuss the cluster, vortical, and compressive IS dipole modes, and proved to be a powerful approach for the IS monopole and dipole excitations in a wide energy range including the low-energy states and high-energy GRs. [44,46].

In our previous work of ^{16}O [42], we have investigated the cluster states with variation after spin-parity projections (VAP) [47] combined with the $^{12}\mathrm{C}+\alpha$-cluster GCM, which we called the VAP+GCM, but not the IS GDR because the sAMD bases have not been adopted in the previous work. The great advantages of the present sAMD+GCM are that it describes both the low-energy cluster state and the GDR in a

unified framework owing to inclusion of one-particle and one-hole (1p-1h) excitations in the sAMD bases, and is suitable to discuss details of the IS dipole excitations. In this paper, we show the IS monopole and dipole strength functions in ^{16}O in a wide energy range covering the low-lying vortical and cluster modes, and also the high-energy compressive vibration modes of the GRs. For detailed analysis of the monopole and dipole transitions, we calculate the form factors and transition densities and compare them with experimental data measured by the electron scattering. We discuss the vortical and cluster aspects of the IS LED states and clarify properties of the IS dipole excitations.

The paper is organized as follows. The formulation of the sAMD+GCM for ^{16}O is explained in Sec. II. Section III shows the calculated results and discusses the properties of the IS monopole and dipole modes. Finally, the paper is summarized in Sec. IV. In the Appendix sections, the definitions of the transition operators, densities, and strengths are given.

II. FORMULATION

In order to calculate the IS monopole and dipole excitations in ^{16}O, we combine the sAMD with the previous VAP+GCM model [42]. Namely, we prepare the sAMD wave functions and combine them with the basis wave functions adopted in the previous VAP+GCM calculation. We call the present calculation sAMD+GCM. In this section, we explain the framework and procedure of the present calculations of ^{16}O. For details of the VAP+GCM and the sAMD, the reader is referred to Refs. [42,44,46,48] and references therein.

A. VAP+GCM with AMD wave functions

An AMD wave function is given by a Slater determinant of single-particle Gaussian wave functions,

$$\Phi_{\rm AMD}(\boldsymbol{Z}) = \frac{1}{\sqrt{A!}}\mathcal{A}\{\varphi_1, \varphi_2, \ldots, \varphi_A\}, \tag{1}$$

$$\varphi_i = \phi_{X_i}\chi_i\tau_i, \tag{2}$$

$$\phi_{X_i}(\boldsymbol{r}_j) = \left(\frac{2\nu}{\pi}\right)^{3/4} \exp\{-\nu(\boldsymbol{r}_j - \boldsymbol{X}_i)^2\}, \tag{3}$$

$$\chi_i = \left(\frac{1}{2} + \xi_i\right)\chi_\uparrow + \left(\frac{1}{2} - \xi_i\right)\chi_\downarrow. \tag{4}$$

where $\mathcal{A}$ is the antisymmetrizer, ϕ_{X_i}, χ_i, and τ_i are the spatial, spin, and isospin functions of the ith single-particle wave function, respectively. The isospin part is fixed to be up (proton) or down (neutron). ν is the width parameter, which is fixed to be $\nu = 0.19$ fm^{-2} used in the previous calculation. The condition $\sum_{i=1,\ldots,A} \boldsymbol{X}_i/A = 0$ is always kept and the contribution of the center of mass motion is exactly removed from the total system. The AMD wave function is specified by the set of variational parameters $\boldsymbol{Z} \equiv \{\boldsymbol{X}_1, \ldots, \boldsymbol{X}_A, \xi_1, \ldots, \xi_A\}$ for the centroids of single-nucleon Gaussian wave packets and nucleon-spin orientations, which are determined by the energy variation.

It should be stressed that, in the AMD model, the existence of any clusters is not *a priori* assumed because Gaussian centroids, $\boldsymbol{X}_1, \ldots, \boldsymbol{X}_A$, of all single-nucleon wave packets are independently treated as variational parameters. Nevertheless, the model wave function can describe various cluster wave functions, and also shell-model wave functions because of the antisymmetrization of Gaussian wave packets.

To obtain the AMD wave function optimized for the J^π state, the VAP is performed with respect to the variation of $\boldsymbol{Z}$ by

$$\delta\frac{\langle\Phi|H|\Phi\rangle}{\langle\Phi|\Phi\rangle} = 0, \tag{5}$$

for the J^π-projected AMD wave function $\Phi = P^{J\pi}_{MK}\Phi_{\rm AMD}(\boldsymbol{Z})$, where $P^{J\pi}_{MK}$ is the spin-parity projection operator. For the AMD wave function $\Phi^{^{16}{\rm O}}_{\rm AMD}(\boldsymbol{Z})$ of ^{16}O, we perform the VAP with $J^\pi_k = 0^+_{1,2}, 2^+_1, 4^+_{1,2}, 1^-_1, 2^-_1, 3^-_1$, and 5^-_1, and obtain nine configurations of $\Phi^{^{16}{\rm O}}_{\rm AMD}(\boldsymbol{Z}^{\rm opt}_\beta)$ with the parameters $\boldsymbol{Z}^{\rm opt}_\beta$ optimized for each $\beta = J^\pi_k$ state. In the simple VAP calculation, we superpose the nine configurations.

In the GCM calculation, we adopt the $^{12}{\rm C} + \alpha$ cluster wave functions, where the angular momentum projection and internal excitations of the subsystem ^{12}C cluster are considered. We first perform the VAP calculation of the subsystem ^{12}C for three states $^{12}{\rm C}(0^+_1)$, $^{12}{\rm C}(0^+_2)$, and $^{12}{\rm C}(1^-_1)$. Using the obtained ^{12}C-cluster wave functions, the $^{12}{\rm C} + \alpha$ wave function is constructed as done in Ref. [42]. The relative distance d between ^{12}C and α clusters is treated as a generator coordinate. The angular-momentum projection of the subsystem ^{12}C is also practically performed by taking into account rotation of the ^{12}C cluster.

B. sAMD+GCM: Combination of sAMD with VAP+GCM

In addition to the VAP and $^{12}{\rm C} + \alpha$ wave functions, the sAMD wave functions are also superposed to describe 1p-1h excitations on the ground state. Starting from the ground-state wave function $\Phi^{^{16}{\rm O}}_{\rm AMD}(\boldsymbol{Z}^{\rm opt}_{\beta=0^+_1})$ obtained by the VAP, we consider small variations of single-particle wave functions by shifting the Gaussian centroid of each single-particle wave function, $\boldsymbol{X}_i \to \boldsymbol{X}_i + \epsilon\boldsymbol{e}_\sigma$ (the spatial position parameters), of $\boldsymbol{Z}^{\rm opt}_{\beta=0^+_1}$ in the AMD wave function. Here ϵ is an enough small constant, $\boldsymbol{e}_\sigma$ ($\sigma = 1, \ldots, 8$) are unit vectors for eight directions. Spin nonflip and flip states and recoil effects are taken into account as explained in Ref. [44]. Consequently, totally $16A = 256$ bases of the shifted AMD wave functions are superposed in addition to the VAP and $^{12}{\rm C} + \alpha$ wave functions in the sAMD+GCM calculation of 0^+ and 1^- states.

In the present sAMD+GCM calculation, we use the $\Phi^{^{12}{\rm C}}_{\rm AMD}(\boldsymbol{Z}^{\rm opt}_{\beta=0^+_1}) + \alpha$ configuration with the intercluster distances of $d = \{1.2, 2.4, \ldots, 7.2$ fm$\}$ and $\Phi^{^{12}{\rm C}}_{\rm AMD}(\boldsymbol{Z}^{\rm opt}_{\beta=0^+_2,1^-_1}) + \alpha$ configurations with $d = \{1.2, 2.4, \ldots, 4.8$ fm$\}$ to save the computational cost. [$\Phi^{^{12}{\rm C}}_{\rm AMD}(\boldsymbol{Z}^{\rm opt}_{\beta=0^+_1,0^+_2,1^-_1}) + \alpha$ with $d = \{1.2, 2.4, \ldots, 8.4$ fm$\}$ are used in Ref. [36], and $\Phi^{^{12}{\rm C}}_{\rm AMD}(\boldsymbol{Z}^{\rm opt}_{\beta=0^+_1,0^+_2}) + \alpha$ with $d = \{1.2, 2.4, \ldots, 8.4$ fm$\}$ and $\Phi^{^{12}{\rm C}}_{\rm AMD}(\boldsymbol{Z}^{\rm opt}_{\beta=1^-_1}) + \alpha$ with $d = \{1.2, 2.4, \ldots, 4.8$ fm$\}$ are used in Ref. [42].]

The IS0 and IS1 transition strengths are calculated with the 0^+ and 1^- states obtained by the sAMD+GCM. The

TABLE I. Properties of 0^+ states; the binding energy (BE), excitation energies (E_x), rms matter radii (R), and the IS0 matrix elements [$M(E0)$]. The present result (sAMD+GCM) and the VAP and VAP+GCM values from Ref. [42] are shown compared with the experimental data [49]. The experimental value of the rms radius of the ground state is deduced from the experimental charge radius measured by the electron scattering [50].

	VAP	VAP +GCM	sAMD +GCM	Exp
BE (MeV)	123.0	123.5	125.6	127.62
$E_x(0_2^+)$ (MeV)	13.1	9.7	11.6	6.05
$E_x(0_3^+)$ (MeV)		15.3	18.6	12.05
$E_x(0_4^+)$ (MeV)		13.6	15.5	13.6
$E_x(0_5^+)$ (MeV)		18.3	20.6	14.01
$R(0_1^+)$ (fm)	2.69	2.73	2.72	2.55
$R(0_2^+)$ (fm)	2.96	3.29	3.16	
$R(0_3^+)$ (fm)		3.53	3.45	
$R(0_4^+)$ (fm)		3.64	3.21	
$R(0_5^+)$ (fm)		3.53	3.36	
$M(E0;0_1^+ \to 0_2^+)$ (e fm^2)	1.8	3.5	3.8	3.55(0.21)
$M(E0;0_1^+ \to 0_3^+)$ (e fm^2)		3.3	3.9	4.03(0.09)
$M(E0;0_1^+ \to 0_4^+)$ (e fm^2)		4.1	4.1	
$M(E0;0_1^+ \to 0_5^+)$ (e fm^2)		3.0	3.2	3.3(0.7)

form factors and transition densities are also calculated with these operators. As for the IS dipole excitations, transition strengths of the CD and TD operators are also calculated. The definitions of the operators, matrix elements, strengths, form factors, and transition densities are given in Appendixes.

III. RESULTS

A. Structure properties of low-energy levels of 0^+ and 1^- states

The sAMD+GCM result of the binding energy, root-mean-square (rms) matter radii, and excitation energies of low-lying 0^+ states are listed in Table I, and those of the 1_1^- and 1_2^- states are shown in Table II . For comparison, values calculated with the VAP (without the $^{12}\mathrm{C}+\alpha$ nor sAMD bases) and those of the VAP+GCM (without the sAMD bases) are also shown in the tables. These corresponds to the VAP and VAP+GCM calculations presented in the previous paper [42].

Various cluster states are obtained in the excited 0^+ levels in $E \lesssim 20$ MeV. Compared the sAMD+GCM and VAP+GCM, there is no essential difference between the two calculations for these states, because the developed cluster states are dominantly contributed by the GCM bases but not by the sAMD bases. It is not the case for the ground state, but the sAMD+GCM obtains 2 MeV energy gain of the 0_1^+ state compared with the VAP+GCM meaning that the sAMD bases efficiently improve the ground-state correlations. Because of this additional energy gain of the ground state, the relative energy position of the excited 0^+ states are raised up by about 2 MeV in the sAMD+GCM. As a result, the agreement with the experimental energy spectra in the sAMD+GCM is not as good as the VAP+GCM, but it is much better than

TABLE II. Properties of the 1_1^- and 1_2^- states, excitation energies, rms radii, the IS1 strengths, and the EWSR ratio P_{IS1} of the energy-weighted IS1 strengths. The present result of the sAMD+GCM and those of the VAP and VAP+GCM calculations from Ref. [42] are shown compared with the experimental data [49].

	VAP	VAP +GCM	sAMD +GCM	exp
$E_x(1_1^-)$ (MeV)	10.3	9.4	9.6	7.12
$E_x(1_2^-)$ (MeV)	17.0	12.1	14.4	9.59
$R(1_1^-)$ (fm)	2.76	2.87	2.80	
$R(1_2^-)$ (fm)	2.96	3.58	3.37	
$B(\mathrm{IS1};0_1^+ \to 1_1^-)$	124.5	165.5	169.8	
$P_{\mathrm{IS1}}(1_1^-)$	0.042	0.048	0.051	0.42[a]
$B(\mathrm{IS1};0_1^+ \to 1_2^-)$	7.9	2.9	10.2	
$P_{\mathrm{IS1}}(1_2^-)$	0.0044	0.0011	0.0045	

[a]The experimental data of the EWSR ratio $P_{\mathrm{IS1}}(1_1^-)$ is the value from Ref. [6] of α inelastic scattering analysis.

the preceding microscopic cluster model calculations. We note that the calculated fourth 0^+ state with the $^{12}\mathrm{C}(2_1^+)+\alpha$ cluster structure should be assigned to the experimental 0_3^+ state, because the sAMD+GCM and VAP+GCM calculations eventually give the opposite ordering of the 0_3^+ and 0_4^+ states as discussed in the previous paper.

In the calculated 1^- levels, the 1_1^- and 1_2^- states are obtained in $E < 15$ MeV. The higher state (1_2^-) is the well-developed cluster state and regarded as the band-head state of the $K^\pi = 0^-$ $^{12}\mathrm{C}+\alpha$ band, which is the parity doublet of the $K^\pi = 0_2^+$ $^{12}\mathrm{C}+\alpha$ band built on the band-head 0_2^+ state. The lower state (1_1^-) has the small rms radius comparable to that of the ground state and shows less prominent cluster structure than the 1_2^- and $0_{2,3,4,5}^+$ states. Comparing with the VAP+GCM, the sAMD+GCM gives the smaller radius of the 1_1^- state. Moreover, the excitation energy of the 1_1^- state is almost same between the sAMD+GCM and VAP+GCM calculations indicating that the sAMD bases describe additional correlations contributing the size shrinkage and the 2 MeV energy gain comparable to that of the ground state.

B. Cluster structures of low-lying states

Cluster aspects of the low-lying states have been investigated in Ref. [42]. We here briefly review the cluster structures of the 0_1^+, 0_2^+, 1_1^-, and 1_2^- states following the discussions in the previous paper based on the analysis of the intrinsic wave functions, $\Phi^{^{16}\mathrm{O}}_{\mathrm{AMD}}(\boldsymbol{Z}^{\mathrm{opt}}_{\beta=J^\pi_k})$, obtained by the VAP calculation.

Figure 1 shows the intrinsic density distribution of the 0_1^+, 0_2^+, and 1_2^- states. The 0_1^+ state shows the tetrahedral 4α cluster structure, in which three αs form the triangle shape on the X-Y plane and the last α cluster is sitting on the Z (vertical) axis [Fig. 1(a)]. Its cluster development is not so remarkable as seen in the compact density distribution. The 1_1^- state also has a tetrahedral 4α clustering with a compact density distribution similar to the 0_1^+ state, but the orientation of the triangle 3α part is somewhat tilted from the 0_1^+. This tilting motion of the triangle 3α produces the dipole excitation with

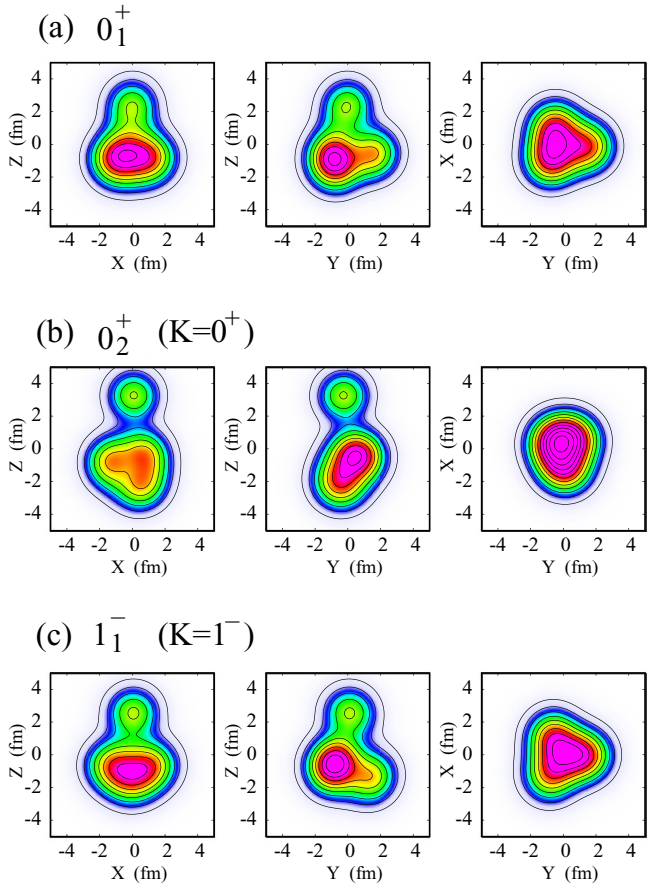

FIG. 1. Density distributions in the intrinsic states obtained by the VAP for the 0_1^+, 0_2^+, and 1_1^- states. The densities integrated along the Y, X, and Z axes are plotted on the (left) X-Z, (middle) Y-Z, and (right) X-Y planes, respectively. Figures corresponds to those of Ref. [42], but are reconstructed from the wave functions.

$K^\pi = 1^-$ in the 1_1^-. This mode is similar to the vibration mode of the tetrahedral 4α discussed by the algebraic 4α cluster model [51,52]. However, the 0_1^+ and 1_1^- states obtained in the present calculation are not the equilateral tetrahedral states but the prolately deformed one with the $3\alpha + \alpha$ configuration and contain the α breaking component.

The 0_2^+ state has the developed $^{12}\mathrm{C} + \alpha$ cluster structure, in which 4α clusters are arranged in a planarlike configuration. Because of the remarkably developed $^{12}\mathrm{C} + \alpha$ clustering, the 0_2^+ state shows a largely deformed intrinsic density compared with the 0_1^+. The developed $^{12}\mathrm{C} + \alpha$ clustering constructs the $K^\pi = 0^+$ band and the parity-partner $K^\pi = 0^-$ band starting from the the band-head 1_2^- state.

We should note that, even though the 0_1^+, 0_2^+, 1_1^-, and 1_2^- show the formation of four α clusters, the clusters are not necessarily the ideal α clusters with the $(0s)^4$ configuration but contain the α-cluster breaking because of the spin-orbit interaction. We can evaluate the α-cluster breaking component from the expectation value of the squared proton spin $\langle \boldsymbol{S}_p^2 \rangle$ because it measures the $S = 1$ mixing induced by the the α breaking. The values calculated with the VAP are $\langle \boldsymbol{S}_p^2 \rangle = 0.07$, 0.71, 0.35, and 0.79 for the 0_1^+, 0_2^+, 1_1^-, and 1_2^-, respectively,

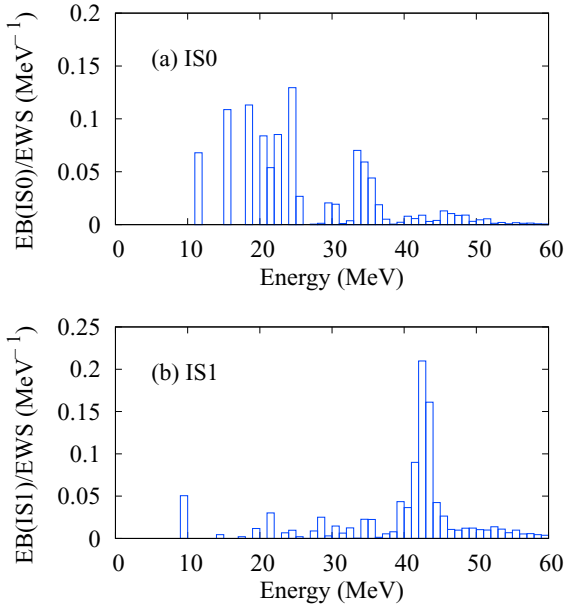

FIG. 2. The EWSR ratio of the IS0 and IS1 transition strengths calculated with the sAMD+GCM.

indicating the slight breaking in the 0_1^+ and the significant α breaking in the 0_2^+, 1_1^-, and 1_2^-.

It should be also commented that these VAP configurations couple with other configurations such as the ^{12}C-cluster rotation and 1p-1h excitations in the sAMD+GCM calculation, but they still give significant contributions and roughly describe main properties of the 0_1^+, 0_2^+, 1_1^-, and 1_2^- states.

C. Transition strengths

The calculated IS0 and IS1 transition strengths to the $0_{2,3,4,5}^+$ and $1_{1,2}^-$ states are listed in Tables I and II. Here the strengths $B(E0) = B(\mathrm{IS0})/4$ are compared with the experimental data. The observed $B(E0)$ of the 0_2^+, 0_3^+, and 0_5^+ state are reproduced well by the sAMD+GCM calculation. In the dipole excitations, the remarkably large $B(\mathrm{IS1})$ is obtained for the 1_1^- with the energy weighted sum rule ratio of 5%, whereas the much weaker IS1 transition is obtained for the 1_2^- state in the $^{12}\mathrm{C} + \alpha$ band. The relatively weak IS1 transition to the cluster state seems to contradict the naive expectation that the compressive operator could excite cluster states, but it is not true for the case of the 1_2^- state. As mentioned previously, the 1_2^- state in the $^{12}\mathrm{C} + \alpha$ band has the planarlike configuration and shows the different orientation of the triangle ^{12}C cluster from the initial 0_1^+. Therefore, the 0_1^+ to 1_2^- excitation involves not only the intercluster excitation but also the ^{12}C-cluster rotation, which can not be directly excited by the IS1 operator.

The IS0 and IS1 strength functions up to $E = 60$ MeV are shown in Fig. 2. The energy-weighted sum rule ratios calculated with the sAMD+GCM are plotted. In the IS0 strength function, a large fraction of the strengths are distributed in $E \leqslant 40$ MeV. The cluster states significantly contribute to the lower part of the strengths in $E \leqslant 20$ MeV, which are not clearly separated from the GMR strengths. On the other hand, in the IS1 strength function, the 1_1^- state contributes to the

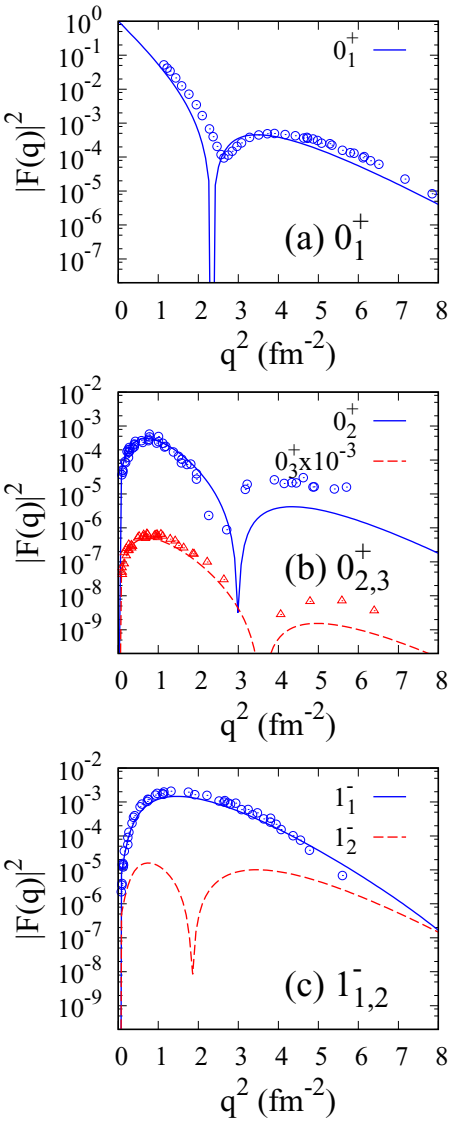

FIG. 3. The elastic and inelastic form factors of the IS0 and IS1 transitions calculated with the sAMD+GCM. The experimental data are electron scattering form factors from Ref. [53].

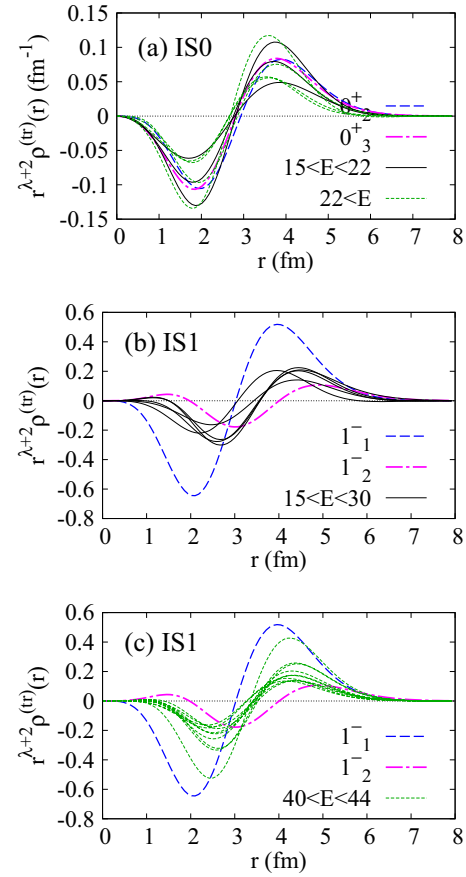

FIG. 4. Transition densities of the IS0 and IS1 transitions, $0^+_1 \to 0^+_k$ and $0^+_1 \to 1^-_k$, calculated with the sAMD+GCM. The densities for the transitions with significant strengths as $B(\mathrm{IS0}: 0^+_1 \to 0^+_k) \geqslant 10$ fm^4 and $B(\mathrm{IS1}: 0^+_1 \to 1^-_k) \geqslant 10$ fm^6 are plotted. The transition densities for the first and second excited states are shown by blue dashed and magenta dash-dotted lines, respectively. The IS0 transition density of 0^+ states in $15 < E < 22$ MeV and the IS1 transition density of 1^- states in $15 < E < 30$ MeV are shown by black solid lines in (a) and (b) and those of the 0^+ states in $22 < E$ MeV and 1^- states in $40 < E < 44$ MeV are shown by green dotted lines in (a) and (c).

significant low-energy strength separated from the IS GDR peak around 40 MeV.

D. Form factors and transition densities

Figure 3 shows the calculated elastic and inelastic form factors of the IS0 and IS1 transitions from the ground state to the $0^+_{1,2,3}$ and $1^-_{1,2}$ states in comparison with experimental data observed by electron scattering [53]. The calculated form factors of the $0^+_{1,2,3}$ states are in good agreement with the experimental data in the low-momentum region. In the shape of the observed inelastic form factors, a difference can be seen between the 0^+_2 and 0^+_3 states. The form factor of the 0^+_2 drops off at the smaller transfer momentum q than the 0^+_3 reflecting the broader radius dependence of the transition density of the 0^+_2. This trend is qualitatively described in the present calculation and understood by the difference in the cluster structures between the 0^+_2 and 0^+_3 states: the dominant $^{12}\mathrm{C}(0^+_1) + \alpha$ component in the 0^+_2 state and the $^{12}\mathrm{C}(2^+_1) + \alpha$ component in the 0^+_3 state.

For the dipole transition to the 1^-_1, the magnitude and shape of the experimental form factor are nicely reproduced by the present calculation. Compared to the 1^-_1, the calculated IS1 transition to the 1^-_2 is quite weak. At the maximum peak, the form factor of the $0^+_1 \to 1^-_2$ transition is about two orders less than that of the $0^+_1 \to 1^-_1$ transition. Moreover, the shape of the form factor is different between the 1^-_1 and 1^-_2 states because of the structure difference. The form factor of the 1^-_2 in the $^{12}\mathrm{C} + \alpha$ band shows a two-peak structure with a dip at $q \approx 2$ fm^{-2}, which can not be seen in the form factor of the 1^-_1 state with the compact tetrahedral 4α.

For further discussions of the IS0 and IS1 transitions, we show the transition densities for the 0^+ and 1^- states with $B(\mathrm{IS0}) > 10$ fm^4 and $B(\mathrm{IS1}) > 10$ fm^6 in Fig. 4. The transition density of the 0^+ states in Fig. 4(a) shows qualitatively

similar behavior with one node around $r = 2.5$–3.0 fm, but one can see a quantitative difference between the 0_2^+ and high-energy 0^+ states. The transition density in the 0_2^+ state is expanded outward and its node is located at the largest position $r \approx 3$ fm due to the developed $^{12}\mathrm{C}(0_1^+) + \alpha$ cluster structure. Conversely, the transition density of higher states in $E > 22$ MeV is contracted inward. This trend can be understood by the character of small amplitude vibration in the high-energy monopole excitations. The transition density for other 0^+ states in $15 < E < 22$ MeV shows the intermediate feature.

Compared with the monopole transitions, the IS1 transition density sensitively reflects different characters of dipole excitations. In particular, one can see clear differences in the transition density between the 1_1^-, 1_2^-, and high-energy GDR. The transition density in the 1_1^- with the compact 4α structure shows the most contracted distribution with a node at $r < 3$ fm and the surface peak at $r \approx 4$ fm. On the other hand, in the 1_2^- state assigned to the $^{12}\mathrm{C} + \alpha$ band, the transition density has two nodes and shows the broadly stretched distribution with the surface peak at $r \approx 5$ fm. In the high-energy GDR transition, which is contributed by the 1^- states in $40 < E < 44$ MeV, the transition density shows the intermediate feature with one node at $r \approx 3.5$ fm and the surface peak at $4 \lesssim r \lesssim 4.5$ fm. In $15 < E < 30$ MeV, most of the 1^- states have the GDR-like transition density but a few states show the 1_1^--like contracted behavior.

E. Vortical nature of dipole excitations

In order to clarify properties of the LED and GDR states, we calculate the transition strengths with the CD and TD operators. Note that the CD strength, which is in principle equivalent to the IS1 strength, is sensitive to the compression dipole mode, whereas the TD strength can probe the nuclear vorticity in the dipole excitation.

The calculated CD and TD strength functions are shown in Fig. 5. In the CD transitions, we obtain the significant strength below 10 MeV for the 1_1^- state and the huge peak around $E = 40$ MeV for the IS GDR. In contract to the CD strength, there is no remarkable TD strength in the high-energy region for the IS GDR. From this result, it is concluded that the IS GDRs do not have the vortical feature but is the normal compressive mode. Instead, the TD strength is concentrated

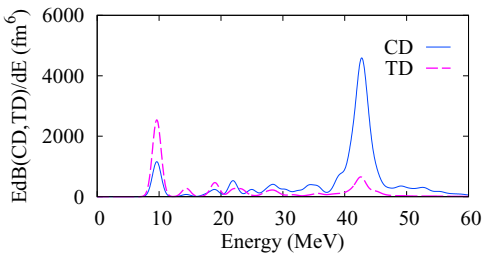

FIG. 5. The energy weighted strength functions of the CD and TD transitions calculated with the sAMD+GCM. The scaled strengths $\tilde{B}(D)$ of discrete states are smeared by Gaussian with the range $\gamma = 1/\sqrt{\pi}$ MeV.

on the 1_1^- state probing the vortical nature. The 1_2^- in the $^{12}\mathrm{C} + \alpha$ band has the weak CD and TD transitions because this state is the intercluster excitation involving the ^{12}C-cluster rotation and is weakly excited by the CD and TD operators.

The present result indicates quite different characters of the dipole excitations between the 1_1^-, 1_2^-, and IS GDR states: the strong CD and TD transitions in the 1_1^-, weak CD and TD transitions in the 1_2^-, and strong CD but weak TD transitions in the IS GDR. In particular, one of the prominent features of the 1_1^- is the strong TD strength. In the analysis of the intrinsic wave functions, we find that the TD strength in the $0_1^+ \to 1_1^-$ is contributed by the dominant $K = 1$ component of the prolately deformed $3\alpha + \alpha$ structure of the 1_1^-. On the other hand, the CD strength in the $0_1^+ \to 1_1^-$ is mainly contributed by the $K = 0$ component. In the 4α structure, the $K = 1$ and $K = 0$ components have large overlap and mixes to each other because of the bosonic symmetry of α clusters. This is a unique feature of the dipole excitation in ^{16}O, in which the 1_1^- state has the strong TD and CD strengths.

To illustrate the vortical and compressive natures of the 1_1^-, we show in Fig. 6 the transition current density of the $0_1^+ \to 1_1^-$ transition in the intrinsic frame calculated using the wave functions $\Phi^{^{16}\mathrm{O}}_{\mathrm{AMD}}(\boldsymbol{Z}^{\mathrm{opt}}_{\beta=0_1^+})$ and $\Phi^{^{16}\mathrm{O}}_{\mathrm{AMD}}(\boldsymbol{Z}^{\mathrm{opt}}_{\beta=1_1^-})$ obtained by the VAP. Here, the transition current density before the K and parity projections at the $Y = 0$ and $X = 0$ planes, [Figs. 6(c) and 6(d)] that after the K projection before the parity projection, and [Figs. 6(e) and 6(f)] that after the K and parity projections are shown. The nuclear matter density of the 0_1^+ and 1_1^- states are also shown by solid and dashed lines, respectively. Note that, the parity (axial) symmetry is broken in the intrinsic states before the parity projection (K projection) but it is restored after the projection.

In the transition current density before the K and parity projections, a vortex is created at the lower part by the tilting motion of the triangle 3α in the tetrahedral 4α configuration as seen in Fig. 6(a) and 6(b). After the $K = 1$ projection, where the nuclear current is averaged around the Z axis, a $K = 1$ vortex appears clearly at the bottom part of Fig. 6(c). Then, after the parity projection, the vortical current is duplicated and two vortices appear in the bottom and top parts. The $K = 1$ vortices aligned along the prolate deformation is the feature of the $K = 1$ VD mode in the prolately deformed system. This mode differs from the torus-shape vortex, which has been originally proposed in the $K = 0$ dipole excitation (obviously, the torus current is allowed only in the $K = 0$ dipole excitation because of the mathematical condition.) The geometrical shape of the current in the $K = 1$ VD mode is described in detail in our previous paper [54].

Let us turn to the nuclear current in the $K = 0$ component shown in Figs. 6(d) and 6(f) before and after the parity projection, respectively. The $0_1^+ \to 1_1^-$ excitation also contains the relative motion between the last α cluster and the 3α. In the $K = 0$ component, this corresponds to the $L = 1$ excitation of the 3α-α relative distance. The relative oscillation of the last α cluster against the 3α induces the compressive nuclear current as seen in Figs. 6(d) and 6(f) and contributes to the significant CD strength in the $0_1^+ \to 1_1^-$ transition.

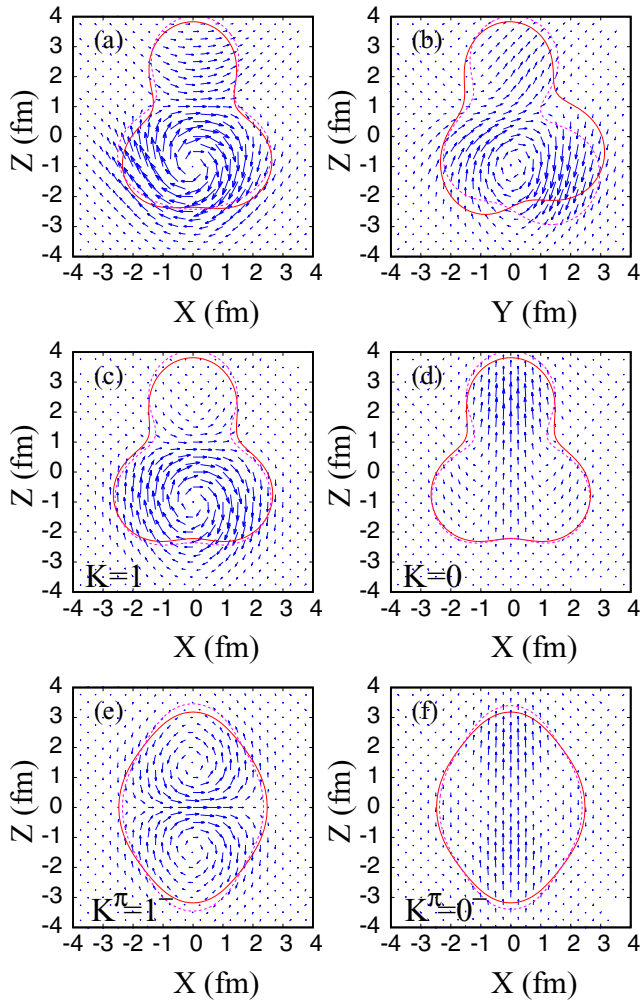

FIG. 6. Transition current density of the $0_1^+ \to 1_1^-$ in the intrinsic frame calculated using the wave functions $\Phi^{^{16}\mathrm{O}}_{\mathrm{AMD}}(\boldsymbol{Z}^{\mathrm{opt}}_{\beta=0_1^+})$ and $\Phi^{^{16}\mathrm{O}}_{\mathrm{AMD}}(\boldsymbol{Z}^{\mathrm{opt}}_{\beta=1_1^-})$ obtained by the VAP. The vector plot of the transition current density before the K and parity projections at the (a) $Y = 0$ on the X-Z plane and (b) $X = 0$ on the Y-Z plane, (c), (d) that after the K projection before the parity projection, and (e), (f) after the K and parity projections are shown. Red solid and magenta dashed lines indicate contours for the matter densities $\rho(X, 0, Z) = 0.08$ fm^{-3} of the initial (0_1^+) and final (1_1^-) states, respectively.

Strictly speaking, it is not be able to uniquely define the intrinsic frame for physical states with eigenvalues of angular momentum, but in the present case that the system has the prolate deformation because of the tetrahedral $3\alpha + \alpha$ configuration, the discussion in the intrinsic frame can be useful to get the intuitive understanding.

IV. SUMMARY AND OUTLOOK

The IS monopole and dipole excitations in ^{16}O were investigated with the sAMD+GCM. The significant IS0 and IS1 transition strengths were obtained in the low-energy region in addition to the GRs. The 1_1^- state contributes to the significant low-energy strength of the IS1 transition with 5% of the energy-weighted sum rule, which describes well the experimental data observed by α inelastic scattering. The calculated form factors of the inelastic transitions to the 0_2^+, 0_3^+, and 1_1^- states reproduce the experimental electron scattering form factors. The transition densities were also analyzed.

The different characters of the dipole excitations were found in the 1_1^-, 1_2^-, and IS GDR: the strong CD and TD transitions in the 1_1^-, the weak CD and TD transitions in the 1_2^-, and the strong CD but weak TD transitions in the IS GDR. Cluster and vortical aspects of the low-energy dipole states were investigated. In conclusion, we regard the 1_1^- as the vortical vibration mode with the tetrahedral 4α structure, the 1_2^- as the $^{12}\mathrm{C} + \alpha$ cluster mode, and the IS GDR as the collective vibration of the compressive dipole mode.

ACKNOWLEDGMENTS

The authors would like to thank the Dr. Nesterenko and Dr. Chiba for fruitful discussions. The computational calculations of this work were performed by using the supercomputer in the Yukawa Institute for theoretical physics, Kyoto University. This work was supported by Grants-in-Aid of the Japan Society for the Promotion of Science (JSPS) (Grants No. 18K03617 and No. 18J20926 and Grants-in-Aid of the Ministry of Education,Culture,Sports,Science and Technology (MEXT) (Grants No. 18H05407).

APPENDIX A: TRANSITION DENSITIES

The density and current density operators for the nuclear matter are defined as

$$\rho(\boldsymbol{r}) = \sum_k \delta(\boldsymbol{r} - \boldsymbol{r}_k), \tag{A1}$$

$$\boldsymbol{j}(\boldsymbol{r}) = -\frac{i\hbar}{2m} \sum_k \nabla_k \delta(\boldsymbol{r} - \boldsymbol{r}_k) + \delta(\boldsymbol{r} - \boldsymbol{r}_k)\nabla_k. \tag{A2}$$

Here, $\boldsymbol{j}(\boldsymbol{r})$ includes only the convection term of the nuclear current but not the spin term of magnetization. The transition density and current density for the $|0\rangle \to |f\rangle$ transition are given as

$$\rho^{(\mathrm{tr})}_{0\to f}(\boldsymbol{r}) = \langle f|\rho(\boldsymbol{r})|0\rangle, \tag{A3}$$

$$\delta\boldsymbol{j}(\boldsymbol{r}) = \langle f|\boldsymbol{j}(\boldsymbol{r})|0\rangle. \tag{A4}$$

The λth transition density is obtained from the multipole decomposition of the transition density,

$$\rho^{(\mathrm{tr})}_{0\to f}(\boldsymbol{r}) = \frac{1}{\sqrt{2J_f + 1}} \sum_\lambda \rho^{(\mathrm{tr})}_{\lambda;0\to f}(r) \tag{A5}$$

$$\times \sum_\mu Y^*_{\lambda\mu}(\hat{\boldsymbol{r}})(J_i M_i \lambda\mu | J_f M_f), \tag{A6}$$

where J_i and M_i (J_f and M_f) are the spin quantum numbers of the initial $|0\rangle$ (final $|f\rangle$) state. The λth multipole component of the so-called longitudinal form factor is related to the Fourier-Bessel transform of the transition charge density $\rho^{\mathrm{ch}}_{\lambda;0\to f}(r)$ by

$$F(q) = \frac{\sqrt{4\pi}}{Z} \frac{1}{\sqrt{2J_i + 1}} \int dr r^2 j_\lambda(qr) \rho^{\mathrm{ch}}_{\lambda;0\to f}(r), \tag{A7}$$

where $\rho^{\rm ch}_{\lambda;0\to f}(r)$ is calculated by taking into account the proton charge radius and assuming the mirror symmetry.

APPENDIX B: IS MONOPOLE AND DIPOLE OPERATORS AND TRANSITION STRENGTHS

The standard compressive-type ISλ operators of the IS monopole and dipole excitations are defined as

$$M_{\rm IS0} \equiv \int d\boldsymbol{r}\rho(\boldsymbol{r})r^2, \tag{B1}$$

$$M_{\rm IS1}(\mu) \equiv \int d\boldsymbol{r}\rho(\boldsymbol{r})r^3Y_{1\mu}(\hat{\boldsymbol{r}}). \tag{B2}$$

The IS0 and IS1 transition strengths for $|0^+_1\rangle \to |J^\pi_k\rangle$ are given by the reduced matrix elements as

$$B({\rm IS}\lambda) = \frac{1}{2J_i+1}\left|\left\langle J^\pi_k\right||M_{\rm IS\lambda}||0^+_1\right\rangle\right|^2, \tag{B3}$$

where the angular momentum of the initial state is J_i and that of the final state is $J^\pi_k = 0^+_k$ and 1^-_k for $\lambda = 0$ and 1, respectively. The reduced matrix elements are related to the transition densities as

$$\left\langle J^\pi_k\right||M_{\rm IS\lambda}||0^+_1\rangle = \sqrt{4\pi}\int drr^2r^{\lambda+2}\rho^{\rm (tr)}_{\lambda;0\to f}(\boldsymbol{r}) \tag{B4}$$

for the IS0 transition and

$$\left\langle J^\pi_k\right||M_{\rm IS\lambda}||0^+_1\rangle = \int drr^2r^{\lambda+2}\rho^{\rm (tr)}_{\lambda;0\to f}(\boldsymbol{r}) \tag{B5}$$

for the IS1 transition.

The energy-weighted sum rule of the IS0 operator is

$$\sum_k (E_k - E_0)B({\rm IS0};0^+_1 \to 0^+_k) = \frac{2\hbar^2A}{m}\langle r^2\rangle \tag{B6}$$

with the mean square radius $\langle r^2\rangle = \langle 0^+_1|\sum_i r_i^2|0^+_1\rangle/A$ of the ground state. For the IS1 operator, we use the following energy-weighted sum rule from Ref. [6],

$$\sum_k (E_k - E_0)B({\rm IS1};0^+_1 \to 1^-_k) = \frac{3\hbar^2A}{32m\pi}\left(11\langle r^4\rangle - \frac{25}{3}\langle r^2\rangle^2 - 10\epsilon\langle r^2\rangle\right), \tag{B7}$$

where $\langle r^4\rangle = \langle 0^+_1|\sum_i r_i^4|0^+_1\rangle/A$ and $\epsilon = (4/\mathcal{E}_2 + 5/\mathcal{E}_0)\hbar^2/3mA$. Here $\mathcal{E}_2$ and $\mathcal{E}_0$ are the IS GQR and GMR energies, for which the empirical values of $\mathcal{E}_2 = 63A^{-1/3}$ MeV and $\mathcal{E}_0 = 80A^{-1/3}$ MeV are used, respectively.

APPENDIX C: CD AND TD STRENGTHS

In the analysis of isoscalar dipole excitations, the CD and TD operators are used as done in Refs. [43,46]. The former (CD) corresponds to the standard IS1 operator and sensitive to the compressive dipole excitations, and the latter (TD) has been proved to be a good measure of the nuclear vorticity in the dipole excitations as discussed in Ref. [14]. They are defined as

$$M_{\rm CD}(\mu) = \frac{-i}{2\sqrt{3}c}\int d\boldsymbol{r}\boldsymbol{j}(\boldsymbol{r})\cdot\left[\frac{2\sqrt{2}}{5}r^2\boldsymbol{Y}_{12\mu}(\hat{\boldsymbol{r}}) - r^2\boldsymbol{Y}_{10\mu}(\hat{\boldsymbol{r}})\right], \tag{C1}$$

$$M_{\rm TD}(\mu) = \frac{-i}{2\sqrt{3}c}\int d\boldsymbol{r}\boldsymbol{j}(\boldsymbol{r})\cdot\left[\frac{\sqrt{2}}{5}r^2\boldsymbol{Y}_{12\mu}(\hat{\boldsymbol{r}}) + r^2\boldsymbol{Y}_{10\mu}(\hat{\boldsymbol{r}})\right], \tag{C2}$$

where $\boldsymbol{Y}_{\lambda L\mu}$ is the vector spherical harmonics.

The matrix elements of these IS dipole operators for the $|0^+_1\rangle \to |1^-_k\rangle$ transitions are given as

$$\langle 1^-_k|M_{\rm CD}(\mu)|0^+_1\rangle = \frac{-i}{2\sqrt{3}c}\int d\boldsymbol{r}\delta\boldsymbol{j}(\boldsymbol{r})\cdot\left[\frac{2\sqrt{2}}{5}r^2\boldsymbol{Y}_{12\mu}(\hat{\boldsymbol{r}}) - r^2\boldsymbol{Y}_{10\mu}(\hat{\boldsymbol{r}})\right], \tag{C3}$$

$$\langle 1^-_k|M_{\rm TD}(\mu)|0^+_1\rangle = \frac{-i}{2\sqrt{3}c}\int d\boldsymbol{r}\delta\boldsymbol{j}(\boldsymbol{r})\cdot\left[\frac{\sqrt{2}}{5}r^2\boldsymbol{Y}_{12\mu}(\hat{\boldsymbol{r}}) + r^2\boldsymbol{Y}_{10\mu}(\hat{\boldsymbol{r}})\right]. \tag{C4}$$

Using the continuity equation, the CD matrix element is related to the matrix element of the standard IS1 operator $M_{\rm IS1}$ as

$$\langle 1^-_k|M_{\rm CD}(\mu)|0^+_1\rangle = -\frac{E}{10\hbar c}\langle 1^-_k|M_{\rm IS1}(\mu)|0^+_1\rangle. \tag{C5}$$

The CD and TD strengths, which are scaled with the factor $(\frac{10\hbar c}{E})^2$, are defined as

$$\tilde{B}({\rm CD,TD};0^+_1 \to 1^-_k) \equiv \left(\frac{10\hbar c}{E}\right)^2|\langle 1^-_k||M_{\rm CD,TD}||0^+_1\rangle|^2. \tag{C6}$$

[1] M. N. Harakeh and A. van der Woude, *Giant Resonances* (Oxford University Press, Oxford, 2001).

[2] N. Paar, D. Vretenar, E. Khan, and G. Colo, Rept. Prog. Phys. **70**, 691 (2007).

[3] T. Aumann and T. Nakamura, Phys. Scr. T **152**, 014012 (2013).
[4] D. Savran, T. Aumann, and A. Zilges, Prog. Part. Nucl. Phys. **70**, 210 (2013).
[5] A. Bracco, F. C. L. Crespi, and E. G. Lanza, Eur. Phys. J. A **51**, 99 (2015).
[6] M. N. Harakeh and A. E. L. Dieperink, Phys. Rev. C **23**, 2329 (1981).
[7] P. Decowski, H. P. Morsch, and W. Benenson, Phys. Lett. B **101**, 147 (1981).
[8] T. D. Poelhekken, S. K. B. Hesmondhalgh, H. J. Hofmann, A. van der Woude, and M. N. Harakeh, Phys. Lett. B **278**, 423 (1992).
[9] S. F. Semenko, Sov. J. Nucl. Phys. **34**, 356 (1981).
[10] D. G. Ravenhall and J. Wambach, Nucl. Phys. A **475**, 468 (1987).
[11] D. Vretenar, N. Paar, P. Ring, and T. Nikšić, Phys. Rev. C **65**, 021301(R) (2002).
[12] N. Ryezayeva *et al.*, Phys. Rev. Lett. **89**, 272502 (2002).
[13] P. Papakonstantinou, V. Y. Ponomarev, R. Roth, and J. Wambach, Eur. Phys. J. A **47**, 14 (2011).
[14] J. Kvasil, V. O. Nesterenko, W. Kleinig, P.-G. Reinhard, and P. Vesely, Phys. Rev. C **84**, 034303 (2011).
[15] A. Repko, P.-G. Reinhard, V. O. Nesterenko, and J. Kvasil, Phys. Rev. C **87**, 024305 (2013).
[16] J. Kvasil, V. O. Nesterenko, W. Kleinig, and P.-G. Reinhard, Phys. Scripta **89**, 054023 (2014).
[17] V. O. Nesterenko, J. Kvasil, A. Repko, W. Kleinig, and P.-G. Reinhard, Phys. Atom. Nucl. **79**, 842 (2016).
[18] V. O. Nesterenko, A. Repko, J. Kvasil, and P. G. Reinhard, Phys. Rev. Lett. **120**, 182501 (2018).
[19] V. M. Dubovik and A. A. Cheshkov, Sov. J. Part. Nucl. **5**, 318 (1975).
[20] T. Yamada, Y. Funaki, T. Myo, H. Horiuchi, K. Ikeda, G. Ropke, P. Schuck, and A. Tohsaki, Phys. Rev. C **85**, 034315 (2012).
[21] Y. Chiba, M. Kimura, and Y. Taniguchi, Phys. Rev. C **93**, 034319 (2016).
[22] J. A. Wheeler, Phys. Rev. **52**, 1083 (1937); **52**, 1107 (1937).
[23] D. M. Dennison, Phys. Rev. **96**, 378 (1954).
[24] D. M. Brink, H. Friedrich, A. Weiguny, and C. W. Wong, Phys. Lett. B **33**, 143 (1970).
[25] Y. Suzuki, Prog. Theor. Phys. **55**, 1751 (1976).
[26] Y. Suzuki, Prog. Theor. Phys. **56**, 111 (1976).
[27] Y. Fujiwara *et al.*, Prog. Theor. Phys. Suppl. **68**, 29 (1980).
[28] M. Libert-Heinemann, D. Baye, and P.-H. Heenen, Nucl. Phys. A **339**, 429 (1980).
[29] W. Bauhoff, H. Schultheis, and R. Schultheis, Phys. Rev. C **29**, 1046 (1984).
[30] P. Descouvemont, Nucl. Phys. A **470**, 309 (1987).
[31] P. Descouvemont, Phys. Rev. C **44**, 306 (1991).
[32] P. Descouvemont, Phys. Rev. C **47**, 210 (1993).
[33] K. Fukatsu and K. Katō, Prog. Theor. Phys. **87**, 151 (1992).
[34] Y. Funaki, T. Yamada, H. Horiuchi, G. Röpke, P. Schuck, and A. Tohsaki, Phys. Rev. Lett. **101**, 082502 (2008).
[35] Y. Funaki, T. Yamada, A. Tohsaki, H. Horiuchi, G. Röpke, and P. Schuck, Phys. Rev. C **82**, 024312 (2010).
[36] Y. Kanada-En'yo, Phys. Rev. C **89**, 024302 (2014).
[37] W. Horiuchi and Y. Suzuki, Phys. Rev. C **89**, 011304(R) (2014).
[38] Y. Kanada-En'yo, H. Horiuchi, and A. Ono, Phys. Rev. C **52**, 628 (1995).
[39] Y. Kanada-En'yo and H. Horiuchi, Phys. Rev. C **52**, 647 (1995).
[40] Y. Kanada-En'yo and H. Horiuchi, Prog. Theor. Phys. Suppl. **142**, 205 (2001).
[41] Y. Kanada-En'yo, M. Kimura, and A. Ono, Prog. Theor. Exp. Phys. **2012**, 01A202 (2012).
[42] Y. Kanada-En'yo, Phys. Rev. C **96**, 034306 (2017).
[43] Y. Kanada-En'yo, Phys. Rev. C **93**, 024322 (2016).
[44] Y. Kanada-En'yo, Phys. Rev. C **93**, 054307 (2016).
[45] M. Kimura, Phys. Rev. C **95**, 034331 (2017).
[46] Y. Kanada-En'yo, Y. Shikata, and H. Morita, Phys. Rev. C **97**, 014303 (2018).
[47] Y. Kanada-En'yo, Phys. Rev. Lett. **81**, 5291 (1998)
[48] Y. Kanada-En'yo and Y. Shikata, Phys. Rev. C **95**, 064319 (2017).
[49] D. R. Tilley, H. R. Weller, and C. M. Cheves, Nucl. Phys. A **564**, 1 (1993).
[50] I. Angeli and K. P. Marinova, At. Data Nucl. Data Tables **99**, 69 (2013).
[51] R. Bijker and F. Iachello, Phys. Rev. Lett. **112**, 152501 (2014).
[52] R. Bijker and F. Iachello, Nucl. Phys. A **957**, 154 (2017).
[53] T. N. Buti *et al.*, Phys. Rev. C **33**, 755 (1986).
[54] Y. Shikata, Y. Kanada-En'yo, and H. Morita, Prog. Theor. Exp. Phys. **2019**, 063D01 (2019).